STRUCTURAL BIOLOGY

Toxin:antitoxin ratio sensing autoregulation of the *Vibrio cholerae parDE2* module

Gabriela Garcia-Rodriguez[1,2]†, Yana Girardin[1,2], Ranjan Kumar Singh[1,2], Alexander N. Volkov[1,2,3], Jeroen Van Dyck[4], Gopinath Muruganandam[1,2]‡, Frank Sobott[5], Daniel Charlier[6]*, Remy Loris[1,2]*

The *parDE* family of toxin-antitoxin (TA) operons is ubiquitous in bacterial genomes and, in *Vibrio cholerae*, is an essential component to maintain the presence of chromosome II. Here, we show that transcription of the *V. cholerae parDE2* (V*cparDE*) operon is regulated in a toxin:antitoxin ratio–dependent manner using a molecular mechanism distinct from other type II TA systems. The repressor of the operon is identified as an assembly with a 6:2 stoichiometry with three interacting ParD2 dimers bridged by two ParE2 monomers. This assembly docks to a three-site operator containing 5′- GGTA-3′ motifs. Saturation of this TA complex with ParE2 toxin results in disruption of the interface between ParD2 dimers and the formation of a TA complex of 2:2 stoichiometry. The latter is operator binding–incompetent as it is incompatible with the required spacing of the ParD2 dimers on the operator.

INTRODUCTION

Toxin-antitoxin (TA) systems, initially discovered as plasmid maintenance systems, are small operons that are ubiquitous in the genomes of bacteria and archaea [for a review, see (*1*)]. Nearly all bacterial and archaeal chromosomes sequenced to date contain one or multiple copies of TA loci (*2*, *3*), with some species, like the persistent pathogen *Mycobacterium tuberculosis*, showing more than 80 predicted TA loci on its chromosome [for a review, see (*4*)]. Despite a lingering controversy regarding their true biological functions (*5*, *6*), a role in bacterial stress response, genome stabilization, and protection against bacteriophages is most often proposed (*5*, *7*–*16*).

TA loci often localize within mobile DNA elements, such as integron platforms within transposons, conjugative plasmids, or (defective) prophages, possibly reflecting a role in the stabilization of such elements (*7*, *17*–*21*). The superintegron on chromosome II of *Vibrio cholerae* is a hotspot containing at least 17 distinct TA systems that are suspected to contribute to its stability (*18*, *21*). Among these are three *parDE*-type systems that mediate degradation of chromosome I upon loss of chromosome II (*22*).

In contrast to gene cassettes on integron platforms in general (*23*, *24*), such TA cassettes seem to contain their own promoter [for a review, see (*25*)]. This strengthens the hypothesis of their role in the stabilization of these long genomic regions. Furthermore, these regions are generally nonessential for bacterial survival, especially under vegetative growth, but rather enhance virulence and confer adaptive potential to environmental pressures (*20*, *22*).

The *parDE* TA family is one of the earliest families that were discovered, its archetype being the *parDE* module on plasmid RK2 (RK2*parDE*) (*26*, *27*). The ParE toxin of the latter was identified as a Gyrase inhibitor (*28*), an activity that was also confirmed for *V. cholerae* ParE2 (*Vc*ParE2) (*29*). The epitope targeted by *Vc*ParE2 is different from the one that is targeted by F-plasmid CcdB, another Gyrase inhibitor of TA origin, but no further structural or mechanistic details are known (*29*). For other ParE family members, their biochemical activities remain unclear. While they exhibit conserved phenotypes in vitro (*22*, *30*) and may influence the effects of quinolone antibiotics on gyrase (*31*), in vitro interaction with gyrase cannot always be demonstrated (*32*).

TA systems have been shown to adopt a variety of complex mechanisms to control transcription and toxin activity. In most cases, the antitoxin plays a major role in autoregulation, either free or in complex with its cognate toxin [for a recent review, see (*33*)]. Although the *parDE* family of TA systems is ubiquitous on bacterial chromosomes (*2*, *34*), little is known about how toxin activity or transcription is regulated. The N-terminal domain of ParD typically folds in a ribbon-helix-helix (RHH) DNA binding structure (*35*–*37*), except for *Escherichia coli* OH157 PaaA2 that lacks such a domain (*38*). The intrinsically disordered C-terminal domain of ParD plays a role in interaction with ParE, wrapping around this partner by folding upon binding (*32*, *36*, *37*, *39*, *40*).

Transcription regulation has been studied for some *parDE* loci in vivo and indicates highly specific interactions (*22*, *41*–*43*). However, only limited in vitro data are now available for the isolated *RK2*ParD and *Vc*ParD2 (*26*, *44*). The early work on plasmid RK2 *parDE* suggested that ParD alone can act as a repressor for the operon (*26*), but it is not known whether the ParE toxin modulates this action. Here, we present the structure and DNA binding of the *V. cholerae* ParDE2 repressor complex and derive a model for the regulation of the Vc*parDE* operon involving a distinct mechanism.

RESULTS

VcParD2 and VcParE2 form a complex with 6:2 stoichiometry

The purified complex of *Vc*ParD2 and *Vc*ParE2 (from hereon *Vc*ParDE2) was analyzed using native mass spectrometry (MS). A dominant set of peaks agrees with a species of molecular mass 77855.31 Da, which

---

[1] Structural Biology Brussels, Department of Biotechnology, Vrije Universiteit Brussel, Pleinlaan 2, B-1050 Brussel, Belgium. [2] Structural Biology Research Center, Vlaams Instituut voor Biotechnologie, Pleinlaan 2, B-1050 Brussel, Belgium. [3] Jean Jeener NMR Centre, Vrije Universiteit Brussel, Pleinlaan 2, B-1050 Brussel, Belgium. [4] Department of Chemistry, Universiteit Antwerpen, Groenenborgerlaan 171, Antwerpen 2020, Belgium. [5] Astbury Centre for Structural Molecular Biology and School of Molecular and Cellular Biology, University of Leeds, Leeds LS2 9JT, UK. [6] Research Group of Microbiology, Department of Bioengineering Sciences, Vrije Universiteit Brussel, Pleinlaan 2, B-1050 Brussel, Belgium.
*Corresponding author. Email: remy.loris@vub.be (R.L.); dcharlie@vub.be (D.C.)
†Present address: Laboratory of Prof. Pierre Gönczy, School of Life Sciences, EPFL (École Polytechnique Fédérale de Lausanne), Lausanne, Switzerland.
‡Present address: Pole of Pharmacology and Therapeutics, Institute of Experimental and Clinical Research, Université Catholique de Louvain, Avenue Hippocrate 57, 1200 Brussels, Belgium.

corresponds to a 6:2 stoichiometry (theoretical molecular weight of 78.22 kDa) of *Vc*ParD2 to *Vc*ParE2, a ratio that is unique among TA complexes (Fig. 1A). Additional minor peaks show the presence of *Vc*ParD2 monomers (8.8 kDa) and minor species of hetero-trimer of 2:1 stoichiometry (30 kDa) and 4:1 stoichiometry (47.8 kDa) that can be explained as dissociation products of the 6:2 *Vc*ParD2:*Vc*ParE2 hetero-octamer. Very small amounts, approaching noise level, of a *Vc*ParDE2 hetero-tetramer of 2:2 stoichiometry (42.9 kDa) can also be discerned.

The observed molecular weight of 78.2 kDa for the *Vc*ParDE2 complex was further confirmed using size exclusion chromatography coupled with small-angle x-ray scattering (SEC-SAXS) (77.11 kDa estimated from Porod volume) and size exclusion chromatography coupled with multiangle light scattering (SEC-MALS) (72.1 ± 0.6 kDa for the lowest concentration used to 75.5 ± 0.4 kDa for the highest one) (Fig. 1, C and D, and fig. S1B).

VcParE2 prevents further self-oligomerization of VcParD2 in the 6:2 VcParDE2 complex

The overall architecture of the complex *Vc*ParDE2 complex as determined by x-ray crystallography (table S1) shows three *Vc*ParD2 dimers in a linear side-by-side array, with a *Vc*ParE2 monomer bound at the C-terminal intrinsically disordered regions (IDRs) of the two outer *Vc*ParD2 monomers, locking up the complex together in a near-arch shape (Fig. 1B and fig. S2). Folding upon binding of the *Vc*ParD2 IDR to *Vc*ParE2 is very similar to what is observed in other ParD-ParE complexes, confirming a conserved mechanism for ParE neutralization (figs. S2, A to C, and S3) (*32*, *36*, *37*). The negatively

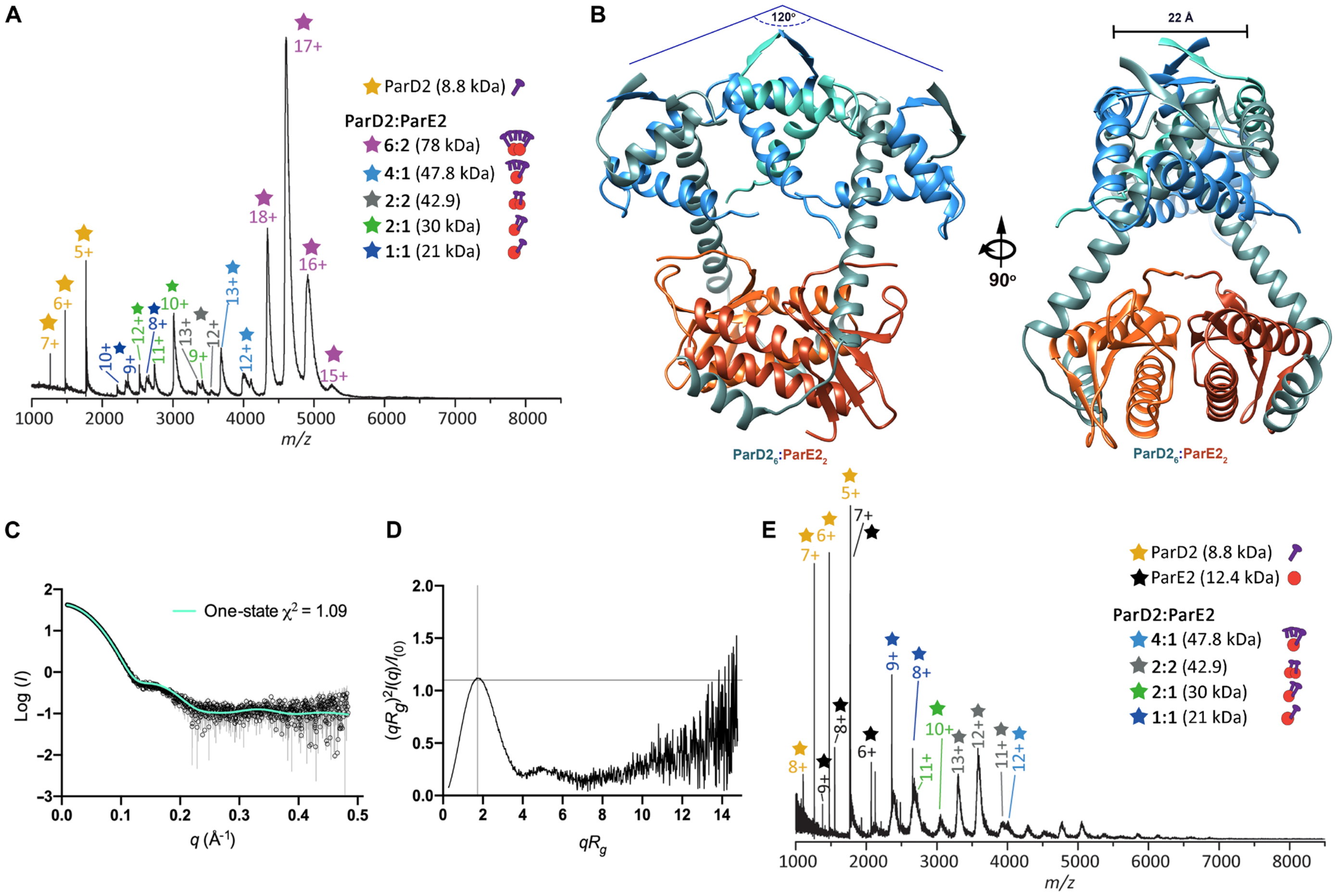

Fig. 1. Mass spectrometry and x-ray crystallography of the *Vc*ParDE2 complex show a 6:2 TA stoichiometry. (**A**) Native mass spectrometry (MS) spectrum of the copurified *Vc*ParDE2 complex. The measured and theoretical masses and charges of the proteins and complexes are indicated with colored stars. Other species likely correspond to small amount of complexes with different stoichiometries: *Vc*ParD2:*Vc*ParE2 (21 kDa), (*Vc*ParD2)$_2$:*Vc*ParE2 (30 kDa), (*Vc*ParD2)$_4$:*Vc*ParE2 (47.8 kDa), and near noise level of (*Vc*ParD2)$_2$:(*Vc*ParE2)$_2$ (42.9 kDa). Diagrams of the different *Vc*ParD2:ParE2 stoichiometries are shown next to the legend. *m/z*, mass/charge ratio. (**B**) Ribbon representation of the 6:2 *Vc*ParD2:ParE2 assembly generated by crystal symmetry. Three *Vc*ParD2 homodimers interact via an inter-homodimer interface to generate a 120° arch. *Vc*ParD2 RHH motifs are located on the surface, which has a width of 22 Å, strongly suggesting this to be the DNA binding site. (**C**) Solution scattering curve of the *Vc*ParDE2 complex from size exclusion chromatography coupled with small-angle x-ray scattering (SEC-SAXS) experiments. The theoretical profile for the *Vc*ParDE2 ensemble generated with all-atom models of the structure shown in (B) is compared with the experimental data (χ^2 = 1.09). (**D**) Kratky plot for the *Vc*ParDE2 complex showing the characteristic features of a globular particle in solution. (**E**) Native MS of the titration of the 6:2 *Vc*ParDE2 complex with additional *Vc*ParE2. Species of molecular weight of 42.9 kDa corresponding to a *Vc*ParDE2 complex of 2:2 stoichiometry as well as free *Vc*ParE2 are now present in larger amounts, while the 6:2 *Vc*ParDE2 complex becomes undetectable.

charged *Vc*ParD2 C terminus interacts with positively charged regions on the surface of the *Vc*ParE2 toxin. In addition, two hydrophobic patches on the surface of *Vc*ParE2 are buried upon antitoxin binding (fig. S3). The remaining four *Vc*ParD2 IDRs remain free and are not observed in the crystal structure (see all-atom model in fig. S1A).

Thus, this architecture is in full accordance with the 6:2 stoichiometry observed in solution. We further validated our crystal structures against the SAXS data by comparing the theoretical scattering profile with the experimental data after modeling in the sequences missing in the crystal structure, which were treated as flexible. The corresponding all-atom ensemble of models agrees with the crystallographic data with χ^2 value of 1.09. Moreover, the Kratky plot of these data displays the characteristic features of a globular particle in solution (Fig. 1, C and D).

The architecture of *Vc*ParD2 dimers within the 6:2 *Vc*ParDE2 complex is reminiscent of the higher oligomeric structure of *Vc*ParD2 in the absence of its *Vc*ParE2 partner (*44*). *Vc*ParD2 dimers oligomerize via an identical interface (size) that is stabilized via salt bridges (fig. S2, E and F). In the absence of *Vc*ParE2, this leads to an association of five to six *Vc*ParD2 dimers into a partial doughnut structure, with further oligomerization being prevented by entropic pressure of the intrinsically disordered tails of the protein (*44*). In the 6:2 *Vc*ParDE2 complex, only three *Vc*ParD2 dimers associate in such a way. Docking of additional *Vc*ParD2 dimers is sterically blocked by the presence of *Vc*ParE2 monomers at both ends of the *Vc*ParD2 hexamer (Fig. 1B and fig. S2F).

The 6:2 *Vc*ParDE2 assembly is further stabilized via contacts between the two *Vc*ParE2 monomers. This interface, which buries a surface area of 850 Å, is rather hydrophobic [Proteins, Interfaces, Structures and Assemblies (PISA) *P* value of 0.357] and predicted to be stable (PISA Δ*iG* of −8.6 kcal/mol) (fig. S2F). Nevertheless, this interface is not stable in solution, as *Vc*ParE2, like all other ParE proteins studied to date, remains monomeric even at high-protein concentration (*44*).

The 6:2 VcParDE2 complex can be titrated with VcParE2 to form a complex with 2:2 stoichiometry

In the *Vc*ParDE2 complex, only two of the six *Vc*ParD2 monomers interact each with a *Vc*ParE2 toxin molecule (Fig. 1B and fig. S2). This suggests that this complex could be further titrated with *Vc*ParE2 to obtain complexes with different toxin:antitoxin stoichiometries. To verify the existence of *Vc*ParDE2 complexes of different stoichiometry, we reconstituted *Vc*ParDE2 from pure *Vc*ParD2 and *Vc*ParE2. Analysis of these reconstitutions on native gels shows the appearance of two different complexes in a ratio-dependent manner (Fig. 2, A and B). One of these species migrates identically to the 6:2 *Vc*ParDE2 complex, while the other one is the only species observed when *Vc*ParD2 and *Vc*ParE2 are mixed at equal molar concentrations. Therefore, this complex likely corresponds to a 2:2 stoichiometry. Further addition of *Vc*ParE2 does not lead to the appearance of additional species except for excess free *Vc*ParE2 that sticks in the wells.

The existence of an alternative 2:2 complex was further confirmed using isothermal titration calorimetry (ITC) (Fig. 2C). Titration of *Vc*ParD2 into *Vc*ParE2 leads to an end stoichiometry of 1, in agreement with a 2:2 complex via the reaction

$$12\ E + D_{12} \rightleftharpoons 6\ E_2D_2 \tag{1}$$

The affinity is very high, and the reaction is enthalpy driven. The thermodynamic parameters [change in Gibbs free energy

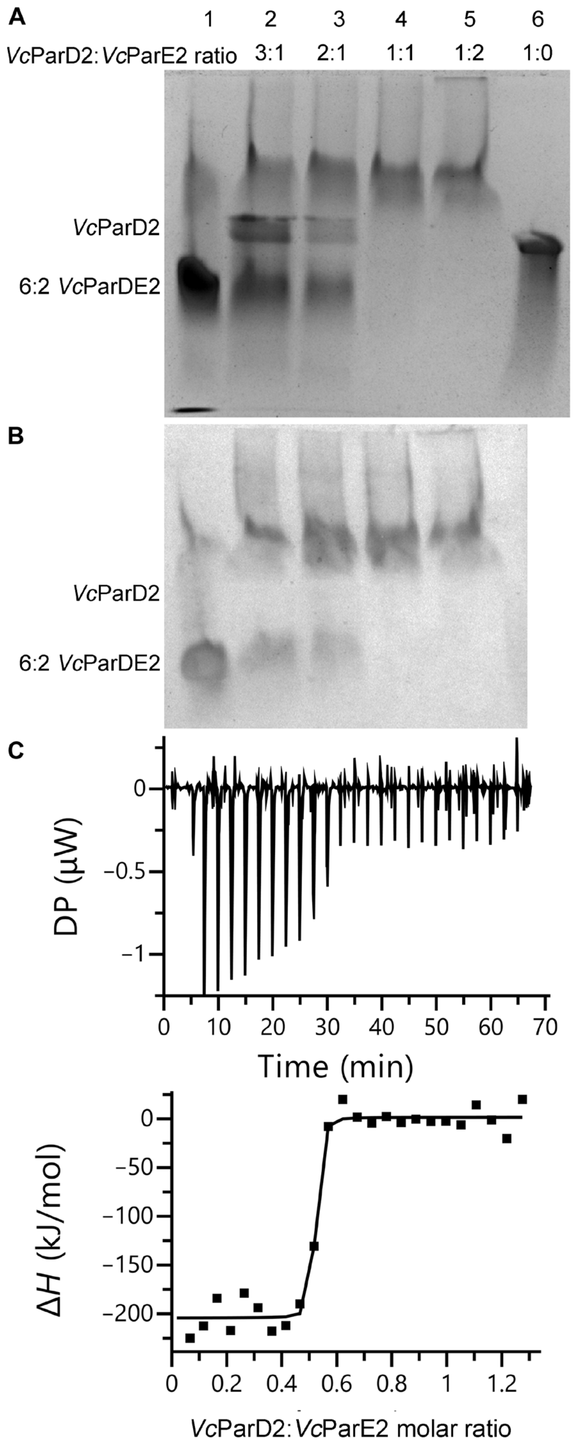

Fig. 2. *Vc*ParD2:ParE2 complex reconstitution from pure *Vc*ParD2 and *Vc*ParE2 proteins shows a saturated 2:2 complex. (**A**) Native polyacrylamide gel electrophoresis of the reconstitution of the *Vc*ParDE2 complex. Lane 1: *Vc*ParDE2 complex purified from coexpression in *E. coli*. Lanes 2 to 5: Reconstituted *Vc*ParDE2 complexes at different molar ratios of *Vc*ParE2 and *Vc*ParD2. Lane 6: Isolated *Vc*ParD2. *Vc*ParD2 and *Vc*ParE2 concentrations are expressed in monomer equivalents. (**B**) Anti-his Western blot of a similar titration visualizing *Vc*ParE2. (**C**) Isothermal titration calorimetry (ITC) titration of *Vc*ParD2 into *Vc*ParE2 resulting in a complex with 2:2 stoichiometry. For this ITC titration, *Vc*ParD2 and *Vc*ParE2 concentrations are expressed in monomer equivalents. DP, differential power.

(ΔG_A) = −11 kcal mol^{-1}; change in enthalpy (ΔH_A) = −23 kcal mol^{-1}; and $T\Delta S_A$ = −12 kcal mol^{-1}, where ΔS_A indicates change in entropy] contain both contributions of the interaction energy between *Vc*ParE2 and *Vc*ParD2 and of the interaction energy between *Vc*ParD2 dimers in the *Vc*ParD2 higher oligomer. However, the tight interaction does not allow to calculate an accurate affinity constant.

To positively identify the species that are formed, we resorted to native MS (Fig. 1E). Titrating additional *Vc*ParE2 into the 6:2 *Vc*ParDE2 complex leads to the appearance of a species of molecular weight of 42.9 kDa corresponding to a *Vc*ParDE2 complex of 2:2 stoichiometry, where *Vc*ParD2 is saturated with *Vc*ParE2. At the same time, the 6:2 *Vc*ParDE2 complex completely disappears when the total antitoxin:toxin ratio exceeds 1.25 (0.5 μM *Vc*ParDE2 and 1.5 μM additional *Vc*ParE2).

Isolated VcParD2 and the 6:2 VcParDE2 complex bind the *parDE2* promoter/operator region

Electrophoretic mobility shift assays (EMSAs) show that both isolated *Vc*ParD2 antitoxin and the 6:2 *Vc*ParDE complex are able to bind a 151–base pair (bp)–long DNA fragment corresponding to the genomic sequence upstream of *parD2* (−60 to +91 with respect to the bacterial promoter prediction program (BPROM) predicted start of transcription) (Fig. 3, A and B). Binding of *Vc*ParD2 results in two distinct concentration-dependent ParD2-DNA complexes with fast migration (Fig. 3A, bands labeled D1 and D2). When more than 6 μM *Vc*ParD2 (dimer equivalents) is incubated with DNA, only one retarded band with migration velocity similar or identical to that of D2 is visible. This band is highly resistant against the presence of competing nonlabeled sonicated salmon sperm DNA, with some effect only seen at a concentration of 2.56 mg ml^{-1} of competitor DNA (fig. S4A).

For the 6:2 *Vc*ParDE2 complex, three concentration-dependent DNA complexes with different migration velocities are observed (Fig. 3B, DE1 to DE3). Of these, bands DE1 and DE2 show practically the same shift as *Vc*ParD2 D1 and D2 bands, respectively. Most likely, at low concentrations, the *Vc*ParDE2 complex dissociates as is also seen in native MS, and these bands are caused by binding of free *Vc*ParD2 dimers to the DNA fragment. The third band, DE3, then likely corresponds to a true *Vc*ParDE2-DNA complex. When *Vc*ParDE2 concentrations surpass 4 μM, only one band is detected that hardly penetrates the gel, likely as a result of aggregation. The DE3 band is more susceptible to the presence of nonspecific competitor DNA than the D2 band formed with *Vc*ParD2. Already from a concentration of 0.4 mg ml^{-1} of salmon sperm DNA, the band starts to disappear (although this still corresponds to a 500-fold excess) (fig. S4B).

A similar pattern is also observed when reconstituting the *Vc*ParDE2 complex from isolated *Vc*ParD2 and *Vc*ParE2. As expected, isolated *Vc*ParE2 toxin does not bind DNA (Fig. 3A). However, when isolated *Vc*ParE2 is added to increasing amounts of *Vc*ParD2 antitoxin before incubation with DNA, a band similar to the DE3 band again appears.

The 6:2 VcParDE2 complex recognizes a 33-bp containing a triple repeat

Deoxyribonuclease (DNase) I footprinting of single-end labeled 151-bp-long control regions does not show protection for *Vc*ParD2, possibly indicating high on- and off-rates. In contrast, DNase I footprinting of the copurified *Vc*ParDE2 complex revealed an approximately 33-nt-long protection zone, from position −21 to +13 on the top (coding) strand and from −22 to +10 on the bottom (template) strand (numbering relative to transcription start) (Fig. 3D). Analysis of the sequence of this protected zone shows the presence of three 5′-GGTA-3′ motifs.

Hyperreactivity for DNase I on both strands, near the extremities of the protected regions, suggests local *Vc*ParDE2-induced DNA bending (minor groove widening). Additional information on critical base and groove-specific contacts was gathered by premodification binding interference (depurination and depyrimidation) and purine methylation protection experiments. The latter indicates the specific recognition of the guanines in the three motives. Depurination and depyrimidation, on the other hand, confirm specificity for the central 29 bp containing the 5′-GGTA-3′ motives. Particularly clear are the interactions with thymines −4 and −14 and adenine −5 on the bottom strand, which lie within the central and the upstream motif (Fig. 3D and figs. S5 and S6).

To further characterize the binding of the *Vc*ParDE2 complex and free *Vc*ParD2, we performed ITC measurements using 39- and 33-bp fragments containing the three motifs (Table 1 and fig. S7). Titration of the 39-bp DNA fragment into a *Vc*ParD2 solution shows an entropy-driven binding of three *Vc*ParD2 dimers with a moderate affinity around 1 μM. In contrast, titration of *Vc*ParDE2 with the same DNA fragment leads to a five times tighter affinity via a similar decrease in both ΔH and $T\Delta S$. Shortening the DNA fragment to 33 bp does not notably affect these parameters.

To further validate the importance of the three 5′-GGTA-3′ motifs, we mutated them individually and together to 5′-ACAC-3′ (Table 1 and fig. S7). Mutation of the middle motif or of all three motifs results in 15- and 30-fold weaker binding, while mutating the two outer motifs only affects binding 1.4- to 1.8-fold.

Together, these experiments show that *Vc*ParD2 specifically recognizes three 5′-GGTA-3′ motifs in the genomic region upstream of *parD2*. The binding of *Vc*ParD2 in complex with toxin *Vc*ParE2 to this DNA fragment is five times stronger than the binding of the antitoxin alone.

A structural model for the VcParDE2-operator complex can be constructed on the basis of structural similarity

A model for the *Vc*ParDE2-operator complex was constructed on the basis of the structure of CopG bound to a 22-bp double-stranded DNA oligonucleotide fragment (see Materials and Methods for details) (*45*). The arrangement of the two adjacent dimers of CopG on its operator is highly similar to the arrangement of *Vc*ParD2 dimers in the isolated *Vc*ParD2 oligomer (*44*) as well as in the *Vc*ParDE2 6:2 complex (fig. S8). Initially, a complex with a 21-bp operator fragment covering two of the three *Vc*ParD2 dimers was generated for which validation with SAXS resulted in a χ^2 value of 1.70 and radius of gyration (R_g) of 30.9 Å for the best-scoring one-state model (Fig. 4A). In this model, the DNA fragment was then extended to cover the full 33-bp operator and the three *Vc*ParD2 dimers. This extended model was validated experimentally using SAXS. The best-scoring two- and three-state models compare to the experimental data with χ^2 values of 9.13 and 9.2, respectively, and with very small differences between R_g values, which oscillate around 32 Å and that arise from different orientations of the disordered ParD2 C termini in solution (Fig. 4B).

In our model, the 5′-GGTA-3′ repeats are located in the operator regions where the *Vc*ParD2 homodimer β sheets get inserted into consecutive major groove segments aligned on one face of the DNA

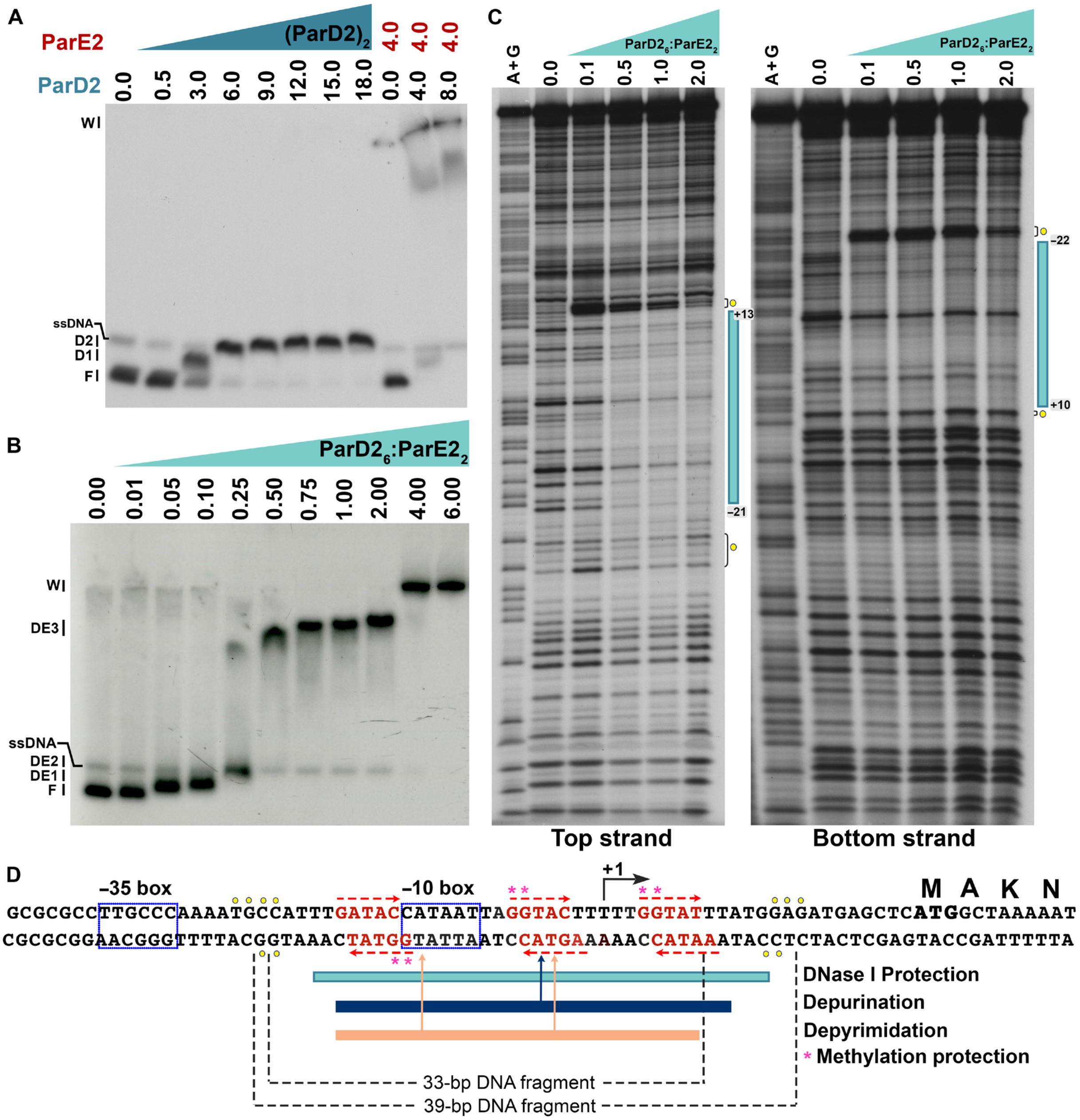

Fig. 3. Isolated *Vc*ParD2 and *Vc*ParDE2 complex bind the *parDE2* promoter/operator region and specifically interact with 5′-GGTA-3′ repeats. Representative autoradiographs of electrophoretic mobility shift assays (EMSAs) with binding of *Vc*ParD2 and *Vc*ParDE2 complex to a [5′-^{32}P] single-end labeled 151-bp DNA fragment, extending from position −60 to +91 with respect to the transcription start of the *parDE2* operon. (**A**) Binding of increasing concentrations of isolated *Vc*ParD2 (dimer equivalent in micromolar) and of isolated *Vc*ParD2 preincubated with *Vc*ParE2 in different stoichiometries. (**B**) Binding of increasing concentrations (indicated in micromolar) of copurified 6:2 *Vc*ParDE2 complex. The position of free DNA (F), single-stranded DNA (ssDNA), the bottom of wells (W), and protein-DNA complexes (DE1 to DE3) with different migration velocities are indicated. (**C**) Autoradiographs of DNase I–footprinting assays with increasing concentrations of copurified *Vc*ParDE2 (in micromolar) to the 151-bp fragment with either the top (coding) or bottom (template) strand as labeled. Filled vertical bars indicate the regions of protection. Positions of hyperreactivity are indicated with a filled yellow circle. A+G corresponds to the Maxam-Gilbert sequencing ladder. (**D**) Sequence of the *parDE2* operator region. +1 indicates the start of transcription; the putative −10 and −35 promoter elements are boxed. Arrows indicate imperfect inverted repeats. The regions protected against cleavage by DNAse I and regions that, upon base-specific modification, negatively interfere with complex formation (see figs. S5 and S6) are indicated with a bar. The 33- and 39-bp fragments used for ITC titrations and SAXS modeling are indicated with dotted lines.

helix and establish sequence-specific interactions via the conserved Lys, Thr, and Ser residues on the N-terminal ribbons (Fig. 4, C and D). Consequently, DNA binding to the symmetric ParD2 homodimers is asymmetric at the level of base contacts: the two β strands originating from each of the monomers of a ParD2 dimer contact different bases, as is also seen for the Arc and CopG operator complexes (*45*–*47*). The GGT motif identified in the DNase I experiment forms a half site that probably confers specificity. The second half site required

Table 1. ITC measurements Standard thermodynamic parameters of association determined via analysis of the ITC data. *Vc*ParD2 concentrations are reported as dimer equivalents, except for the *Vc*ParD2 in *Vc*ParE2 titration where *Vc*ParD2 is considered a monomer. The *n* values for the VcParD2:39-bp DNA interaction indicate a stoichiometry of 3:1. Variant negative (NEG) represents the 39-bp fragment in which all three 5′-GGTA-3′ *VcparDE2* operator motifs are mutated to 5′-ACAC-3′, while variants 1, 2, and 3 have the first, second, and third *VcparDE2* operator motif mutated to 5′-ACAC-3′, respectively.

Interaction	T	n	K_d	ΔG_A	ΔH_A	$T\Delta S_A$
	(K)		(10^{-6} M)	(kcal mol^{-1})	(kcal mol^{-1})	(K kcal mol^{-1})
*Vc*ParD2-*Vc*ParE2	298.15	0.99	–	−11.0 ± 1.0	−23.0 ± 1.0	−12.0 ± 2.0
Operator (39 bp)–*Vc*ParD2	298.15	0.39	0.99 ± 0.11	−8.2 ± 0.1	26.4 ± 0.7	34.6 ± 0.8
Operator (33 bp)–*Vc*ParDE2	298.15	0.97	0.25 ± 0.03	−9.0 ± 0.1	21.2 ± 0.2	30.2 ± 0.3
Operator (39 bp)–*Vc*ParDE2	298.15	0.98	0.18 ± 0.04	−9.3 ± 0.2	23.3 ± 0.6	32.6 ± 0.8
Operator (39 bp) variant NEG–*Vc*ParDE2	298.15	0.98	5.60 ± 2.09	−7.2 ± 0.2	2.68 ± 0.3	9.8 ± 0.5
Operator (39 bp) variant 1–*Vc*ParDE2	298.15	0.94	0.33 ± 0.03	−8.9 ± 0.1	26.6 ± 0.3	35.6 ± 0.4
Operator (39 bp) variant 2–*Vc*ParDE2	298.15	0.95	2.92 ± 0.32	−7.6 ± 0.1	18.1 ± 0.3	25.7 ± 0.4
Operator (39 bp) variant 3–*Vc*ParDE2	298.15	1.06	0.26 ± 0.04	−9.0 ± 0.1	11.0 ± 0.2	20.1 ± 0.3

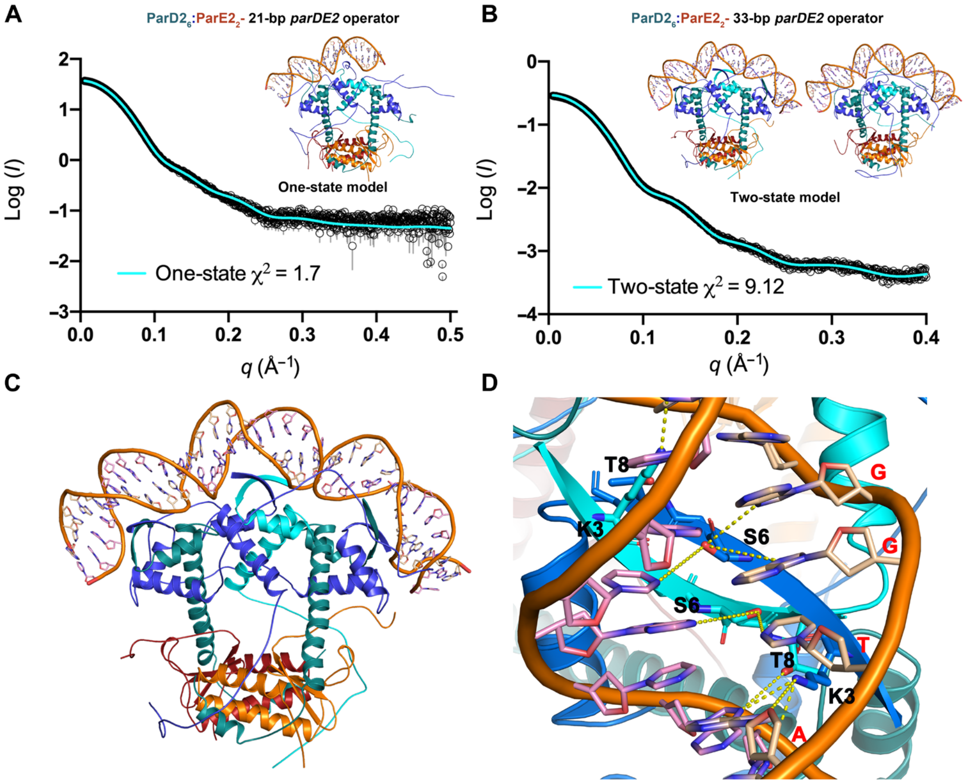

Fig. 4. A structural model for the *Vc*ParDE2-operator complex is validated by SAXS experiments. Solution scattering curve of *Vc*ParDE2 in complex with a 21-bp DNA fragment (**A**) and this same fragment extended up to 33 bp (**B**). Multiple copies of the model of *Vc*ParDE2 in complex with DNA ($n = 1$ to 5), derived to fit the experimental data, were refined simultaneously to simulate molecular ensembles of multiple conformers. The lowest-energy solution with one-state models and two-state models, respectively, are represented as ribbons and the corresponding theoretical SAXS profiles compared to the experimental data (χ^2 values of 1.7 and 9.12, respectively). (**C** and **D**) Ribbon representation of the *Vc*ParDE2 in complex with a 33-bp DNA fragment comprising the three GGTA repeats. The binding of the protein complex induces a 120° arch on the DNA. The *Vc*ParD2 β sheets get inserted into consecutive major groove segments aligned on one face of the DNA helix. The GGTA repeats establish sequence-specific interactions via the conserved Lys, Thr, and Ser residues on the N-terminal ribbons.

for *Vc*ParDE2 binding is not conserved and located either at the 5′ (ATA for site 1) or at the 3′ (ACT or ATT for sites 2 and 3) side of the GGT motif (Fig. 4B and fig. S8B). Such arrangements where a binding site for a dimeric DNA binding protein contains a specific half combined with a nonspecific half are also observed, for example, in the *Pseudomonas putida* GraTA TA operon (*48*).

VcParE2 toxin influences VcParD2 DNA binding activity in a toxin:antitoxin ratio–dependent manner

The presence of non-occupied binding sites for *Vc*ParD2 in the 6:2 *Vc*ParDE2 complex and its conversion into a complex with 2:2 stoichiometry upon titration with *Vc*ParE2 suggest that transcription regulation may be affected by the cellular ratio between *Vc*ParD2 and *Vc*ParE2. To verify this possibility, EMSAs were run where fixed amounts of DNA and 6:2 *Vc*ParDE2 complex were titrated with *Vc*ParE2 (Fig. 5A). When the amount of *Vc*ParE2 equals or exceeds that of *Vc*ParD2 in the mixture, the DE3 band disappears, and only a fast-migrating band similar to the DE2 band remains observed. At lower *Vc*ParDE2 concentrations (where only DE2 is present) and still higher *Vc*ParE2-to-*Vc*ParD2 ratios, the fast-moving bands also disappear, and no DNA binding is detected. In this low *Vc*ParDE2 concentration range, as the concentration of *Vc*ParE2 increases further (especially visible from monomer ratio *Vc*ParE2:*Vc*ParD2 of 1.66), another complex migrating more slowly than DE3 appears, but, simultaneously, DE1 and DE2 disappear and free DNA is generated, indicating that binding of ParD2 is abolished. Higher concentrations of toxin result in slower migration as observed in the lane with ratio 3.33, where the major super-shifted band is migrating even more slowly than that in the lane with ratio 2.0 and even some DNA remains in the well (likely due to aggregation or precipitation). This kind of "stepwise migration" is generally an indication of additional nonspecific DNA binding (fig. S9).

To further evaluate the nature of the corresponding DNA complexes, the complex of 6:2 *Vc*ParDE2 with a 39-bp DNA fragment was titrated with free *Vc*ParE2, and the resulting molecular species were identified using native MS (Fig. 5, B and C). The corresponding mass spectra are dominated by the signal for DNA (which was added in excess to drive binding of 6:2 *Vc*ParDE2), but clear binding of the 6:2 *Vc*ParDE2 complex to this operator fragment is observed, confirming the footprinting, EMSA, and ITC measurements. Upon further titration with *Vc*ParE2, the signal for 6:2 *Vc*ParDE2 bound to DNA weakens and eventually disappears. No alternative DNA complexes with a *Vc*ParD2:*Vc*ParE2 combination of different stoichiometry appear. Furthermore, we do not observe any unbound 6:2 *Vc*ParDE2. Unfortunately, we cannot with certainty observe the buildup of the expected 42.9-kDa 2:2 *Vc*ParDE species as its signals are completely swamped by the very strong signals of the isolated DNA.

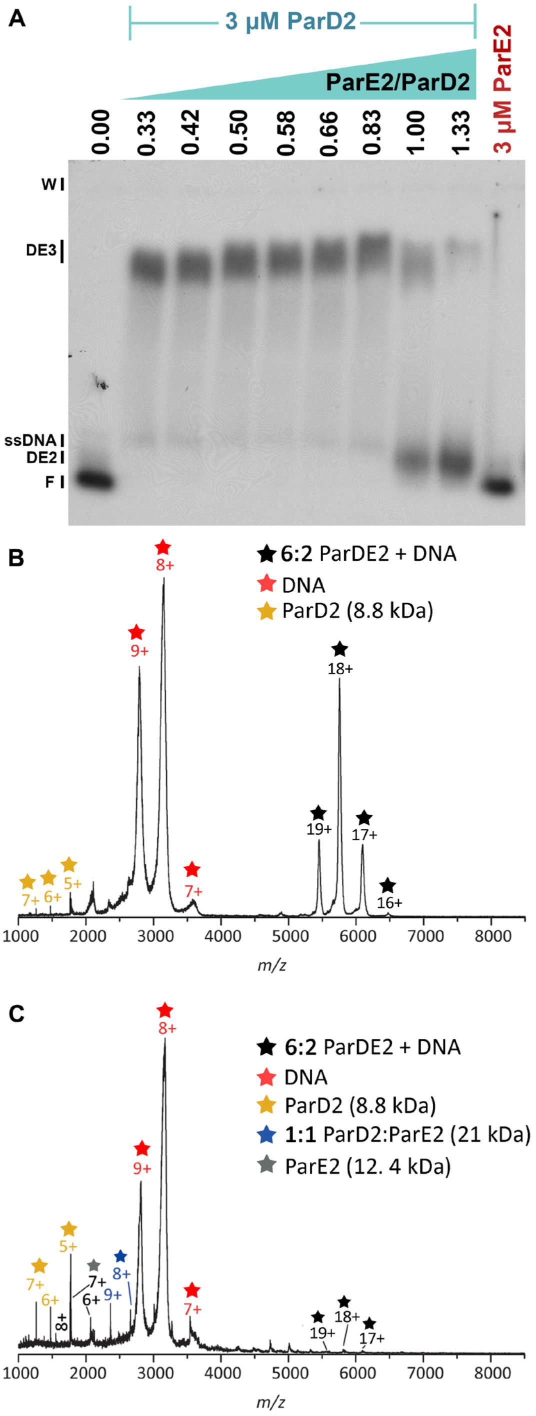

Fig. 5. *Vc*ParE2 influences *Vc*ParD2-DNA binding in a toxin:antitoxin ratio–dependent manner. (**A**) Representative autoradiographs of EMSAs with binding of a constant amount of copurified 6:2 *Vc*ParDE2 corresponding to 3 μM *Vc*ParD2 preincubated with increasing amounts of isolated *Vc*ParE2 resulting in different ParE2/ParD2 ratios as indicated, before incubation with the single-end labeled 151-bp DNA fragment comprising the control region of the *parDE2* operon. (**B**) Native mass spectrum of the *Vc*ParDE2 complex with 2:2 stoichiometry (0.5 μM) in the presence of excess operator fragment (0.75 μM 39-bp DNA duplex). (**C**) Identical experiment, but after titration with 1 μM additional *Vc*ParE2. The charged states are indicated on top of the peaks. The colored stars represent different stoichiometries of the complexes corresponding to the masses detected on the spectra.

DISCUSSION

The *parDE* family of TA systems is one of the earliest families that was identified but, although widespread in bacteria, remains poorly understood in terms of its mechanism of gyrase inhibition as well as its regulation at the level of transcription. Here, we identify the repressor of a *parDE* operon as a ParD-ParE complex with an unusual 6:2 TA stoichiometry. This complex is different from the ParDE complexes with 2:2 stoichiometry that were reported up to now (fig. S3) (*36*, *37*, *39*, *40*). It is also distinct in stoichiometry and architecture from all other repressing complexes of other TA modules such as Phd/Doc, CcdAB, AtaTR, RelBE, HigBA; HicAB, HipBA, and VapBC (*49*–*56*). Why the *Vc*ParDE2 complex has such a fixed 6:2 stoichiometry and does not consist of a set of variants involving two, four, five, and six ParD2 dimers (as could be assumed from the larger oligomer formed when no *Vc*ParE2 is present) (*44*) remains unclear. This may be a consequence of both the ratio at which toxin and antitoxin are produced from the operon, combined with a stabilizing effect of the dimerization of the *Vc*ParE2 toxin in the TA complex. Further in vitro titration of the 6:2 complex with *Vc*ParE2 leads to a "classic" 2:2 complex that loses its DNA binding property. Together, this indicates a ratio-dependent mechanism of transcription regulation as summarized in Fig. 6.

The *Vc*ParD2 oligomer itself [mostly 8-mer or 10-mer; see (*44*)] binds to the *parDE2* operator with an affinity that is only fivefold weaker than that for the *Vc*ParDE2 6:2 complex, indicating that substoichiometric binding of *Vc*ParE2 to *Vc*ParD2 likely does not notably influence the repressor potential of the antitoxin. This agrees with earlier in vivo work where it was established that *Vc*ParD2 is sufficient to repress expression from the P*parD2* promoter (*22*). Thus, *Vc*ParD2 acts as the repressor for the operon that can capture a substoichiometric amount of *Vc*ParE2. The latter would be the situation in vivo and somewhat increases repressor activity (Fig. 6). This is also consistent with early reports on the *parDE* operon on plasmid RK2 as well as more recent data on *parDE2* from *Mycobacteriom smegmatis* that both indicate that, in general, ParD antitoxins on their own are sufficient for repression (*26*, *43*).

When the *VcparDE2* system is activated and the ratio of ParE2 to ParD2 increases, a classic complex with 2:2 stoichiometry is formed. This complex loses its ability to bind DNA and repress the operon (Fig. 6). Presumably, this is due fully to the loss of cooperative binding of *Vc*ParD dimers to adjacent sites. No two *Vc*ParD2 dimers can bind adjacent when sequestered in a 2:2 complex due to steric exclusion (fig. S10), and the affinity of a single *Vc*ParD2 dimer in the context of a 2:2 complex is likely too weak to allow repression. This agrees with our ITC titrations of *Vc*ParD2 with operator fragments containing only a single GGTA motif where no binding is observed (fig. S7G).

In the *Vc*ParDE2 complex, adjacent antitoxin dimers interact directly and strongly with each other through their folded domains in

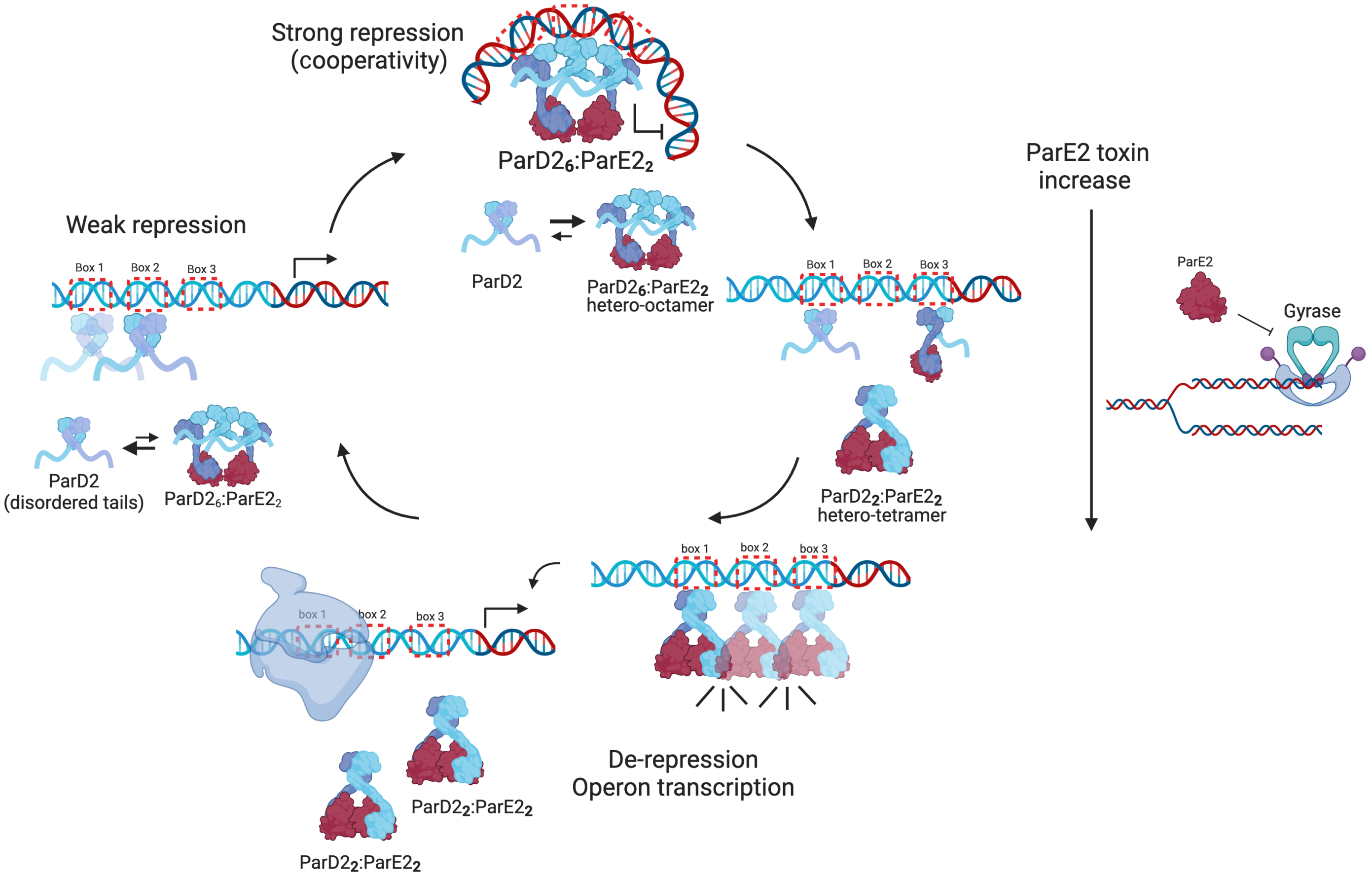

Fig. 6. Schematic model of the regulation of the Vc*parDE2* operon. *Vc*ParD2 antitoxin (shown in shades of blue) exists as RHH homodimers with disordered C termini in solution. In the absence of toxin or at low toxin:antitoxin ratios, *Vc*ParD2 homodimers bind operator boxes (imperfect palindromic repeats) with high dissociation rates or low affinity. Binding of *Vc*ParE2 (shown in red) induces the structuring of *Vc*ParD2 C termini and the preferential stabilization of the 6:2 *Vc*ParD2:ParE2 complex, which pre-orients three antitoxin homodimers in the right orientation for DNA binding via simultaneous contacts with three operator boxes. This complex causes the strongest operator binding and thereby the highest repression of transcription initiation. When toxin:antitoxin ratios increase, more *Vc*ParE2 toxin monomers bind free *Vc*ParD2 C termini in the 6:2 *Vc*ParDE2 assembly and destabilize it. *Vc*ParD2 antitoxin is liberated from this complex and able to weakly bind the operator, therefore restoring some level of transcription. The saturated 1:1 TA heterotetramer is not able to consecutively bind the three operator boxes due to steric hindrance. When all TA complex exists as the saturated 2:2 TA heterotetramer, operator binding is abrogated, and transcription rates increase.

a way similar to what is also observed for the operator complex of the structurally related CopG repressor [where two dimers bind cooperative to the *copG-repB* operator (*47*)]. The cooperative operator binding of CopG is a well-known feature within the RHH superfamily of transcription factors and is also observed, for example, for the Arc repressor or Mnt (*46*, *57*, *58*). In Vc*parDE2*, the IDR region of *Vc*ParD2 adds an additional layer of control, allowing derepression by an additional protein (*Vc*ParE2), a feature that is absent for the RHH regulators outside a TA context.

Evidence that our proposed mechanism of regulation for Vc*parDE2* may be more general comes from the *relBE* systems where the toxin RelE, despite having a different biochemical activity (ribosome-dependent ribonuclease), is structurally related to the ParE gyrase poisons (*36*) and the antitoxin RelB also features a RHH DNA binding domain (*52*). RelE and ParE proteins likely share a common ancestor (*2*). A CopG-like architecture of the *E. coli relBE* repressor complex was also proposed with two RelE dimers docking to adjacent operator sites (*52*), although no experimental structure of a full operator–RelB or operator-RelBE complex is available. Given also the ratio-dependent regulation of *E. coli relBE*, with an antitoxin:toxin complex of 4:2 stoichiometry as the repressing complex and a 2:2 complex as a nonrepressing assembly (*59*), a very similar regulatory mechanism as for Vc*parDE* is likely but now involving only two instead of three binding sites for antitoxin dimers on the operator. Together, this suggests a mechanism that is widespread within the *parDE/relBE* superfamily of TA systems.

Less expected is the similarity with transcription regulation within the *ataRT/kacAT* TA family (*51*, *60*). Here, there is no clear evolutionary relationship with the *parDE/relBE* superfamily except that the antitoxin again contains an RHH-type DNA binding domain. The repressing complex is, like for *E. coli relBE*, of 4:2 stoichiometry and the RHH domains again interact with each other in a CopG-like manner. The corresponding antitoxins AtaR or KacA on their own are insufficient for repression, which may be a consequence of the smaller inter-dimer interface in these TA complexes, reducing cooperativity on DNA binding. The toxin here stabilizes the 4:2 complexes by interacting with two antitoxin dimers at the same time, and, as a consequence, all four IDR regions of the two antitoxin dimers interact with the two toxins in the complex. The 2:2 complex again does not bind DNA and does not repress, making this mechanistically similar to what we see for Vc*parDE* despite differences in detail.

While the mechanism described in this paper may thus be widespread within the TA world, still not all TA systems with RHH-containing DNA binding domain make use of it. For at least two other TA families (*ccdAB* and *vapBC/fitAB*), the antitoxin dimers do not touch each other in the repressing complex but are bridged by the toxin (*50*, *56*, *61*). For *ccdAB*, this also results in ratio-dependent regulation (*62*, *63*), while the details of transcription regulation in the *vapBC* family remain unclear.

In conclusion, the *V. cholerae parDE2* TA system makes use of a unique type of repressor complex that allows ratio-dependent transcription of the operon via disruption of contacts between antitoxin dimers. The underlying mechanism builds upon the regulation known for CopG and related RHH-type transcription factors that function through cooperative interactions of adjacent dimers on their operators. At least two families of TA systems with a different evolutionary origin for their toxins (*parDE/relBE* and *ataRT/kacAT*) have independently extended this repression mechanism in a similar way.

MATERIALS AND METHODS

Protein production

Cloning, expression, and purification of *Vc*ParD2, *Vc*ParE2, and their complex have been described (*44*). *Vc*ParE2 contains a C-terminal histidine tag, while *Vc*ParD2 remains untagged.

Size exclusion chromatography coupled with multiangle light scattering

SEC-MALS experiments were carried out on a high-performance liquid chromatography (HPLC) system (Waters) followed by an in-line connected miniDAWN Treos II (Wyatt Technology) light scattering detector (using three angles) and a Shodex Refractive index detector (RI-501). For the measurements, a shodex-K402.5-4F SEC column equilibrated with 2 to 3 column volumes of running buffer [20 mM tris (pH 8), 150 mM NaCl, and 1 mM tris(2-carboxyethyl) phosphine (TCEP)] was used. Different concentrations of the *Vc*ParD2:*Vc*ParE2 complex, ranging from 10 to 1 mg/ml, were prepared in the same buffer, and 10 μl of each sample was injected in the column. As calibration standard, we applied a bovine serum albumin sample (1 mg/ml). Data processing and molar mass determination were done using the ASTRA 7.1.4 software.

Native polyacrylamide gel electrophoresis

*Vc*ParD2 and *Vc*ParE2-His were mixed at different ratios of monomer equivalents (3:1, 2:1, 1:1, and 1:2) in 20 mM tris (pH 8), 150 mM NaCl, and 1 mM TCEP. The final *Vc*ParE2-His concentration always equaled 10 μM, the one of *Vc*ParD2 was varied (30, 20, 10, and 5 μM) to obtain the desired ratios. Purified *Vc*ParD2:*Vc*ParE2-His complex at 5 μM was used as reference. All protein samples were mixed with an approximate incubation time of 1 hour, combined with native sample buffer [62.5 mM tris-HCl (pH 6.8), 25% glycerol, and 1% bromophenol blue] in a 5:1 ratio and loaded onto a 10% native polyacrylamide gel consisting of separating gel [10% (w/v) acryl/bisacrylamide, 0.25 M tris-HCl (pH 8.8), 0.1% (w/v) ammoniumpersulfate (APS), 0.1% (v/v) *N*,*N*,*N*',*N*'-tetramethylenediamine (TEMED)] and stacking gel [5% (w/v) acryl/bisacrylamide, 0.32 M tris-HCl (pH 8.8), 0.1% (w/v) APS, and 0.1% (v/v) TEMED]. The gel was run in native running buffer (25 mM tris and 192 mM glycine) for 2 hours at 120 V on ice. Subsequently, staining with Coomassie and anti–His-tag Western blot were performed to visualize proteins.

Isothermal titration calorimetry

ITC experiments were performed using the MicroCal PEAQ system. For DNA binding, triplicate experiments were carried out in which the syringe was loaded with a 33- or 39-bp DNA fragment comprising the wild-type *VcparDE2* operator region at concentrations ranging from 245 to 278 μM, while the cell contained *Vc*ParD2:*Vc*ParE2 complex (21.4 to 22.3 μM) or *Vc*ParD2 (50.4 to 67.2 μM dimer equivalents). Similarly, variants of this 39-bp DNA fragment (with the three 5′-GGTA-3′ *VcparDE2* operator motifs mutated individually or all combined to 5′-ACAC-3′) were loaded in the syringe at 450 μM, while the cell contained *Vc*ParD2:*Vc*ParE2 complex at concentrations ranging from 30 to 40 μM. Each 150 s, 18 times in total, 1.5 μl of DNA was injected in the cell. All measurements were carried out in 20 mM tris (pH 8), 150 mM NaCl, and 1 mM TCEP at a stirring speed of 750 rpm and a constant temperature of 25°C. Binding isotherms were analyzed using the MicroCal PEAQ-ITC Analysis Software. The sequences of all used DNA fragments are listed in fig. S7.

For the *Vc*ParE2-*Vc*ParD2 interaction, the cell contained *Vc*ParE2 (6 μM), and the syringe was loaded with *Vc*ParD2 (80 μM monomer equivalent). On the basis of the information of the aggregation state of the interacting proteins (*44*), the ITC curve was described by the following single binding event

$$E + \frac{1}{12}D_{12} \rightleftharpoons \frac{1}{2}E_2D_2 \tag{2}$$

Fitting of the corresponding model function to the ITC curve at a given temperature results in values of the corresponding association (K_A) or dissociation ($K_d = 1/K_A$) constants and standard enthalpies of association (ΔH_A). K_A and K_d are dimensionless thermodynamic equilibrium constant defined in terms of species activities. Because of the applied low-protein concentrations, ideal solution behavior is assumed. Thus, activities are obtained as equilibrium molar species concentration divided by the concentration (1 M) in its standard state. From these data, changes in standard Gibbs free energy (ΔG_A; Eq. 3) and standard entropy (ΔS_A; Eq. 4) associated with the binding event were calculated

$$\Delta G_A = -RT \ln K_A \tag{3}$$

$$\Delta G_A = \Delta H_A - T\Delta S_A \tag{4}$$

Electrophoretic mobility shift assay

A 350-bp-long DNA fragment comprising the first 67 bp of the *parD2* open reading frame (ORF) and extending further upstream in the control region of the *parDE2* operon from *V. cholerae* biovar El Tor strain N16961 (NCBI NC_002506.1) was synthesized by polymerase chain reaction (PCR)–based gene assembly (*64*). The assembled 350-bp fragment was used as the template for PCR amplification of a 151-bp-long fragment comprising the putative operator region upstream of *parD2* ORF with the oligonucleotides forward (Fw) 5′-tgaggcgtttgttatgcgc and reverse (Rv) 5′-tttgtatttggcttgtaataaagccat as primers, of which one was [5′-^{32}P] single-end labeled with (γ-^{32}P)–adenosine 5′-triphosphate (PerkinElmer, 3000 Ci mmol^{-1}) and T4 polynucleotide kinase (Thermo Fisher Scientific) as described (*65*). Labeled PCR fragments were purified by gel electrophoresis on 6% polyacrylamide. For EMSAs, *Vc*ParDE2, *Vc*ParD2, *Vc*ParE2, and reconstituted *Vc*ParDE2 complex were mixed with labeled DNA (10,000 to 15,000 cpm) in 20 mM tris (pH 8), 150 mM NaCl, and 1 mM TCEP (total volume of 20 μl) and incubated at 20°C for 30 min. All binding assays were performed in the presence of an excess nonspecific, nonlabeled competitor DNA (herring sperm DNA, 25 μg ml^{-1}), unless otherwise indicated. After incubation, 3 μl of loading buffer (25% Ficoll, 0.1% xylenexyanol, and 0.1% bromophenol) was added to each sample. Separation was performed on 6% polyacrylamide gels run in tris-boric acid–EDTA buffer at 130 V for approximately 3 hours.

DNase I footprinting

To map the binding site of the *Vc*ParD2:*Vc*ParE2 complex, DNase I–footprinting experiments (*66*) were performed with both the 5′ single-end ^{32}P-labeled forward and reverse strand of a DNA control region (TGAGGCGTTTGTTATGCGCGCCTTGCCCAAAATGCCATTTGATACCATAATTAGGTACTTTTTGGTATTTATGGAGATGAGCTCATGGCTAAAAATACAAGTATCACTCTTGGTGAACACTTCGATGGCTTTATTACAAGCCAAATACAAA). DNA fragments at 150,000 cpm per well were incubated with a dilution series of *Vc*ParD2:*Vc*ParE2 complex (0, 0.1, 0.5, 1, and 2 μM) for 30 min in H_2O at room temperature. A 1:100 dilution of DNAse I (Roche, 10 U/μl) in DNAse I buffer [10 mM cacodylate buffer (pH 8), 10 mM $MgCl_2$, 5 mM $CaCl_2$, and 0.1 mM dithiothreitol] was added to the complex mix at a 1:5 ratio. After 5 min of incubation, DNAse I stop mix (3 M ammonium acetate and 0.25 M EDTA) was added, and DNA was precipitated. Identical counts of the DNA pellet dissolved in formamide dye were loaded on a 6% denaturing polyacrylamide gel [6% (w/v) acrylamide:bisacrylamide ratio 19:1, 89 mM tris, 89 mM boric acid, 2.5 M EDTA, 7 M ureum, 0.1% (w/v) APS, and 0.05% (v/v) TEMED] and a 10% denaturing polyacrylamide gel [idem, but with 10% (w/v) acrylamide:bisacrylamide ratio 19:1] for the labeled reverse and forward strand, respectively. To obtain the sequencing ladders, the protocol explained in (*67*) was followed.

Premodification binding interference

Sparingly modified [5′-^{32}P] single-end labeled DNA (on average, one modification per DNA molecule) for use in premodification binding interference (missing contact) assays (*68*) was generated as described (*67*). Premodified Fw* (top) and Rv* (bottom) labeled-DNA was incubated with 0.1, 0.5, and 2 μM ParD2:ParE2 complex, respectively, as described above for EMSAs, and analyzed by native gel electrophoresis. The resolved free and bound DNA forms corresponding to different complexes were recovered from gel and cleaved at modified positions by piperidine-treatment (*67*), and the reaction products subsequently analyzed by denaturing gel electrophoresis as described above.

Methylation protection

Methylation protection experiments were performed as described (*69*). Single-end Fw* and Rv* labeled DNA (150,000 cpm) was incubated with a dilution series of the VcParD2:VcParE2 complex (0.1, 0.25, 0.5, 1, and 2 μM) respectively, as described above. Limited methylation was performed by the addition of 1 μl of dimethyl sulfate for 1 min at 20°C. The reaction was stopped with 50 μl of stop solution [1.5 M sodium acetate (pH 7.0) and 1.0 M 2-mercaptoethanol] and 15 μg of yeast tRNA. Piperidine-induced strand scission was performed before analysis by denaturing gel electrophoresis. Reference ladders were generated by chemical sequencing of the 151-bp labeled fragment (*67*), and all gels were autoradiographed to display the bands.

Native mass spectrometry

Native MS was performed on a Synapt G2 (Waters, Wilmslow, UK) mass spectrometer. ParDE2 (6:2 complex), ParE, and DNA samples were exchanged into 200 mM ammonium acetate (pH 8.0) through Micro Bio-Spin columns (Bio-Rad, Temse, Belgium), and protein or DNA concentration was determined by nanodrop p2000 (Thermo Fisher Scientific, Merelbeke, Belgium). The sample concentrations were optimized resulting in 0.5 μM for *Vc*ParDE2 and 0.75 μM for DNA. *Vc*ParE2 was added in different concentrations ranging from 0.25 to 2.00 μM and incubated on ice for 5 min. The samples were introduced into the gas phase through nano-electrospray ionization with in-house prepared gold-coated borosilicate glass capillaries. The settings were optimized for the analysis of larger structures as natively as possible, and the critical voltages and pressures used were sampling cone voltage of 50 V and a trap collision energy of 10 V with pressures throughout the instrument of 6.14 and 2.38×10^{-2} mbar for the source and trap collision cell regions.

Analyses of the acquired spectra were performed using Masslynx version 4.1 (Waters, Wilmslow, UK). Native MS spectra were smoothed (extent depending on size of the complexes) and additionally centered for calculating molecular weights to find the precise stoichiometries.

X-ray crystallography

*Vc*ParD2:ParE2 in 20 mM tris-HCl (pH 8), 150 mM NaCl, and 1 mM tris(2-carboxyethyl)phosphine was concentrated to 12 mg ml^{-1}. Crystallization conditions were screened by equilibrating drops of 0.1 μl of protein solution and 0.1 μl of reservoir solution against 100 μl of reservoir solution in sitting drop configuration and, later on, incubated at 293 K. Crystals of the *Vc*ParD2-*Vc*ParE2 complex grew after 2 years using 0.1 M KCl, 0.1 M Na-Hepes (pH 7), and 15% polyethylene glycol 5000 monomethyl ether (PEG 5000 MME) as the precipitant formulation in the reservoir. For data collection, crystals were flash-cooled in liquid nitrogen. Data were collected on PROXIMA-2A at the SOLEIL synchrotron facility, Gif-sur-Yvette, France. All data were indexed, integrated, and scaled with XDS (*70*) via the XDSME interface (*71*). Data quality and twinning were analyzed with phenix.xtriage (*72*) and POINTLESS (*73*).

The structure of the *Vc*ParD2:ParE2 complex was determined by molecular replacement using Phaser-MR. Initially, only a single molecule of *Caulobacter crescentus* ParE (*36*) [Protein Data Bank (PDB) entry 3kxe] could be placed in the AU with log likelihood gain (LLG) and translation function *z*-score (TFZ) values of 34 and 8.4, respectively. This partial solution was refined in phenix.refine, and the refined model was subsequently defined as known partial solution in another Phaser-MR search that located 1.5 dimers of the N-terminal domain of *Vc*ParD2. The resulting model was then refined using phenix.refine (*74*) combined with manual model building in Coot (*75*). Noncrystallographic symmetry and secondary structure restraints were applied throughout. Data collection and refinement statistics for all structures are given in table S1.

Small-angle x-ray scattering

SAXS data were collected at beamline BM29 [European Synchrotron Radiation Facility (ESRF)] in HPLC mode. Shodex KW402.5-4F column was used to collect data for the *Vc*ParD2:ParE2 complex. Superdex 200 Increase column (GE Healthcare) was used to collect data for *Vc*ParD2:ParE2-DNA complexes and DNA samples. Protein samples were prepared as described above for crystallization, concentrated, and briefly spun down before loading onto the SEC column. Twenty-five microliters of *Vc*ParDE2 (18 mg ml^{-1}) was injected onto the Shodex column.

Double-stranded DNA fragments were generated as described above. *Vc*ParD2:ParE2 (100 μM) (6:2) complex was incubated with 50 μM 33- or 21-bp DNA operator variants in 500 μl of final volume (sequences given in the table in fig. S7). Protein-DNA complexes were incubated at 25°C for 15 min before injection onto a Superdex 200 Increase gel filtration column (GE Healthcare). The peak corresponding to DNA-protein complex was collected and concentrated. The concentrated *Vc*ParD2:ParE2-DNA peak (75 μl) and 100 μM DNA samples were injected onto the Superdex 200 Increase 200 connected to the capillary to which the x-rays were directed.

All samples were measured in 20 mM tris (pH 8), 150 mM NaCl, and 1 mM TCEP at 19°C. Constant column flow rates of 0.2 and 0.75 ml min^{-1} were used for the Shodex KW402.5-4F and the Superdex 200 Increase columns, respectively. The final scattering curve (after buffer subtraction) was generated for each sample after a range of scattering curves around the peak (with equivalent R_g values) was normalized and averaged. The R_g values were derived from the Guinier approximation at small q values, while the I_o parameter was estimated by extrapolation to $q = 0$ using the ATSAS suite (*76*). Molecular weights were determined by the Bayesian estimation implemented in Primus (ATSAS suite).

Modeling of the VcParD2:ParE2-DNA complex

Atomic coordinates were taken from the *Vc*ParDE2 structure presented here and the available structure of the transcriptional repressor CopG from *Streptococcus agalactiae* plasmid PMV158, in complex with its 22-bp DNA operator (PDB ID 1ea4). Thus, the RHH motifs of two ParD2 dimers (residues 1 to 40) in the *Vc*ParDE2 complex were superimposed onto the CopG dimers bound to DNA. Subsequently, the bases of the CopG DNA were edited to match the 21-bp DNA fragment used for SAXS. The two palindromic sequences (5′-TGCA-3′) separated by 5 bp in the CopG operator were mutated to the two imperfect palindromes in the *parDE2* operator (5′-GTA[C/T]-3′) separated by 6 bp. This way, a model for a *Vc*ParDE2-DNA complex is obtained where two of the three ParD2 dimers are bound to DNA, the third dimer remaining free.

To generate the complex with the full 33-bp operator fragment, two *Vc*ParDE2-22 bp copies were superimposed to provide a rough estimate to create a continuous 33-bp DNA fragment. The overlapping DNA segments were pruned and connected to form a single 33-bp segment. The sequence of the resulting 33-bp DNA duplex was edited to generate the correct sequence of the 33-bp operator. The resulting model was inspected for steric clashes in Chimera, and energy minimization of the DNA backbone was performed. An angle of approximately 120° was imposed across the entire fragment, as suggested by ab initio models generated with the SAXS data.

In our model, the GGTA repeats are located in regions of the operator where the ParD2 homodimer β sheets get inserted into consecutive major groove segments aligned on one face of the DNA helix and establish sequence-specific interactions via the conserved Lys, Thr, and Ser residues on the N-terminal ribbons. Consequently, DNA binding to the symmetric ParD2 homodimers is asymmetric at the level of base contacts: the two β strands originating from each of the monomers of a ParD2 dimer contact different bases, as is also seen for the Arc and CopG operator complexes (*45*–*47*).

Model refinement against experimental SAXS data

All simulations were performed in Xplor-NIH v 2.49 (*77*, *78*), starting from the x-ray structure of the *Vc*ParDE2 complex determined in this work. Protons and atoms of the residues not resolved in the x-ray structure were added in Xplor-NIH, followed by minimization of the energy function consisting of the standard geometric (bonds, angles, dihedrals, and impropers) and steric (van der Waals) terms. The missing C termini of the four ParD2 protomers as well as the C-terminal histidine tags on *Vc*ParE2 were treated as flexible.

For the refinement against the experimental SAXS data, the positions of the structured protein regions were kept fixed, while the following stretches of residues at the protein termini were given full degree of freedom: first three N-terminal amino acids of ParD2; C-terminal ParD2 residues 49 to 81 (chains B and D), 46 to 81 (chains E and F), and 79 to 81 (chains C and H); and C-terminal ParE2 residues 91 to 105. The computational protocol comprised an initial simulated annealing step followed by the side-chain energy minimization as described before (*79*). In addition to the standard geometric and steric terms, the energy function included a knowledge-based dihedral angle potential and the SAXS energy term incorporating the experimental data (*80*). Truncated SAXS curves ($q < 0.4$ Å^{-1}) were used as the sole experimental input.

For the refinement of the *Vc*ParDE2-DNA complexes, the atomic coordinates were taken from the homology models built in this work (see above). DNA mutations were introduced in Xplor-NIH, followed by the energy minimization of the resulting double-stranded DNA helix. In addition to the standard geometric and steric terms, the energy function included a hydrogen bond potential ensuring correct Watson-Crick pairing and a knowledge-based positional potential for the coplanarity of the complementary bases and their favorable orientation within the DNA double helix (*81*, *82*). Refinement against the SAXS data was performed in the same setup as that described above for the *Vc*ParDE2 system; the positions of the DNA atoms were kept fixed throughout the simulations. For the *Vc*ParDE2 complex with the 33-bp DNA, multiple copies of the molecular system ($n = 1$ to 5) were refined simultaneously to simulate molecular ensembles of multiple conformers (*79*).

In each refinement run, 100 structures were calculated, and 10 lowest-energy solutions, representing the best agreement with the experimental data, were retained for the subsequent analysis. The agreement between the experimental and calculated SAXS curves (obtained with the calcSAXS helper program, which is part of the Xplor-NIH package) was assessed by calculating the χ^2

$$\chi^2 = \frac{1}{n-1}\sum_{i=1}^{n}\left(\frac{I(q)_{\mathrm{calc},i} - I(q)_{\mathrm{exp},i}}{\delta I(q)_{\mathrm{exp},i}}\right)^2 \quad (5)$$

where $I(q)_{\mathrm{calc},i}$ and $I(q)_{\mathrm{exp},i}$ are the scattering intensities at a given q for the calculated and experimental SAXS curves, $\delta I(q)_{\mathrm{exp},i}$ is an experimental error on the corresponding $I(q)_{\mathrm{exp},i}$ value, and n is the number of data points defining the experimental SAXS curve.

Supplementary Materials

The PDF file includes:

Figs. S1 to S10

Tables S1 and S2

Legend for supplemental Excel file

Other Supplementary Material for this manuscript includes the following:

Supplemental Excel file

REFERENCES AND NOTES

1. K. Gerdes, S. K. Christensen, A. Løbner-Olesen, Prokaryotic toxin–antitoxin stress response loci. *Nat. Rev. Microbiol.* **3**, 371–382 (2005).
2. D. P. Pandey, Toxin-antitoxin loci are highly abundant in free-living but lost from host-associated prokaryotes. *Nucleic Acids Res.* **33**, 966–976 (2005).
3. K. S. Makarova, Y. I. Wolf, E. V. Koonin, Comprehensive comparative-genomic analysis of Type 2 toxin-antitoxin systems and related mobile stress response systems in prokaryotes. *Biol. Direct* **4**, 19 (2009).
4. A. Sala, P. Bordes, P. Genevaux, Multiple toxin-antitoxin systems in *Mycobacterium tuberculosis*. *Toxins (Basel)* **6**, 1002–1020 (2014).
5. M. LeRoux, P. H. Culviner, Y. J. Liu, M. L. Littlehale, M. T. Laub, Stress can induce transcription of toxin-antitoxin systems without activating toxin. *Mol. Cell* **79**, 280–292.e8 (2020).
6. N. Fraikin, F. Goormaghtigh, L. Van Melderen, Type II toxin-antitoxin systems: Evolution and revolutions. *J. Bacteriol.* **202**, e00763-19 (2020).
7. S. Szekeres, M. Dauti, C. Wilde, D. Mazel, D. A. Rowe-Magnus, Chromosomal toxin–antitoxin loci can diminish large-scale genome reductions in the absence of selection. *Mol. Microbiol.* **63**, 1588–1605 (2007).
8. F. L. Short, C. Akusobi, W. R. Broadhurst, G. P. C. Salmond, The bacterial type III toxin-antitoxin system, ToxIN, is a dynamic protein-RNA complex with stability-dependent antiviral abortive infection activity. *Sci. Rep.* **8**, 1013 (2018).
9. R. L. Dy, R. Przybilski, K. Semeijn, G. P. C. Salmond, P. C. Fineran, A widespread bacteriophage abortive infection system functions through a type IV toxin–antitoxin mechanism. *Nucleic Acids Res.* **42**, 4590–4605 (2014).
10. F. Hayes, B. Kędzierska, Regulating toxin-antitoxin expression: Controlled detonation of intracellular molecular timebombs. *Toxins* **6**, 337–358 (2014).
11. T. R. Blower, T. J. Evans, R. Przybilski, P. C. Fineran, G. P. C. Salmond, Viral evasion of a bacterial suicide system by RNA–based molecular mimicry enables infectious altruism. *PLOS Genet.* **8**, e1003023 (2012).
12. Y. Otsuka, T. Yonesaki, Dmd of bacteriophage T4 functions as an antitoxin against *Escherichia coli* LsoA and RnlA toxins. *Mol. Microbiol.* **83**, 669–681 (2012).
13. Y. Cui, X. Su, C. Wang, H. Xu, D. Hu, J. Wang, K. Pei, M. Sun, T. Zou, Bacterial MazF/MazE toxin-antitoxin suppresses lytic propagation of arbitrium-containing phages. *Cell Rep.* **41**, 111752 (2022).
14. I. Bleriot, L. Blasco, O. Pacios, L. Fernández-García, A. Ambroa, M. López, C. Ortiz-Cartagena, F. F. Cuenca, J. Oteo-Iglesias, Á. Pascual, L. Martínez-Martínez, P. Domingo-Calap, T. K. Wood, M. Tomás, The role of PemIK (PemK/PemI) type II TA system from *Klebsiella pneumoniae* clinical strains in lytic phage infection. *Sci. Rep.* **12**, 4488 (2022).
15. E. Shmidov, I. Lebenthal-Loinger, S. Roth, S. Karako-Lampert, I. Zander, S. Shoshani, A. Danielli, E. Banin, PrrT/A, a *Pseudomonas aeruginosa* bacterial encoded toxin-antitoxin system involved in prophage regulation and biofilm formation. *Microbiol. Spectr.* **10**, e01182–e01122 (2022).
16. M. LeRoux, M. T. Laub, Toxin-antitoxin systems as phage defense elements. *Annu. Rev. Microbiol.* **76**, 21–43 (2022).
17. E. Krin, Z. Baharoglu, O. Sismeiro, H. Varet, J.-Y. Coppée, D. Mazel, Systematic transcriptome analysis allows the identification of new type I and type II toxin/antitoxin systems located in the superintegron of *Vibrio cholerae*. *Res. Microbiol.* **174**, 103997 (2023).
18. N. Iqbal, A.-M. Guérout, E. Krin, F. Le Roux, D. Mazel, Comprehensive functional analysis of the 18 *Vibrio cholerae* N16961 toxin-antitoxin systems substantiates their role in stabilizing the superintegron. *J. Bacteriol.* **197**, 2150–2159 (2015).
19. A.-M. Guerout, N. Iqbal, N. Mine, M. Ducos-Galand, L. Van Melderen, D. Mazel, Characterization of the *phd-doc* and *ccd* toxin-antitoxin cassettes from Vibrio Superintegrons. *J. Bacteriol.* **195**, 2270–2283 (2013).
20. M. Christensen-Dalsgaard, K. Gerdes, Two *higBA* loci in the *Vibrio cholerae* superintegron encode mRNA cleaving enzymes and can stabilize plasmids. *Mol. Microbiol.* **62**, 397–411 (2006).
21. D. A. Rowe-Magnus, A.-M. Guerout, L. Biskri, P. Bouige, D. Mazel, Comparative analysis of superintegrons: Engineering extensive genetic diversity in the Vibrionaceae. *Genome Res.* **13**, 428–442 (2003).
22. J. Yuan, Y. Yamaichi, M. K. Waldor, The three *Vibrio cholerae* chromosome II-encoded ParE toxins degrade chromosome I following loss of chromosome II. *J. Bacteriol.* **193**, 611–619 (2011).
23. C. M. Collis, R. M. Hall, Site-specific deletion and rearrangement of integron insert genes catalyzed by the integron DNA integrase. *J. Bacteriol.* **174**, 1574–1585 (1992).
24. C. M. Collis, R. M. Hall, Expression of antibiotic resistance genes in the integrated cassettes of integrons. *Antimicrob. Agents Chemother.* **39**, 155–162 (1995).
25. G. Cambray, A.-M. Guerout, D. Mazel, Integrons. *Annu. Rev. Genet.* **44**, 141–166 (2010).
26. R. C. Roberts, C. Spangler, D. R. Helinski, Characteristics and significance of DNA binding activity of plasmid stabilization protein ParD from the broad host-range plasmid RK2. *J. Biol. Chem.* **268**, 27109–27117 (1993).
27. E. P. Johnson, A. R. Strom, D. R. Helinski, Plasmid RK2 toxin protein ParE: Purification and interaction with the ParD antitoxin protein. *J. Bacteriol.* **178**, 1420–1429 (1996).
28. Y. Jiang, J. Pogliano, D. R. Helinski, I. Konieczny, ParE toxin encoded by the broad-host-range plasmid RK2 is an inhibitor of Escherichia coligyrase. *Mol. Microbiol.* **44**, 971–979 (2002).
29. J. Yuan, Y. Sterckx, L. A. Mitchenall, A. Maxwell, R. Loris, M. K. Waldor, *Vibrio cholerae* ParE2 poisons DNA gyrase via a mechanism distinct from other gyrase inhibitors. *J. Biol. Chem.* **285**, 40397–40408 (2010).
30. J. R. Ames, M. Muthuramalingam, T. Murphy, F. Z. Najar, C. R. Bourne, Expression of different ParE toxins results in conserved phenotypes with distinguishable classes of toxicity. *Microbiol. Open* **8**, e902 (2019).
31. M. Muthuramalingam, J. C. White, T. Murphy, J. R. Ames, C. R. Bourne, The toxin from a ParDE toxin-antitoxin system found in *Pseudomonas aeruginosa* offers protection to cells challenged with anti-gyrase antibiotics. *Mol. Microbiol.* **111**, 441–454 (2019).
32. Y. G.-J. Sterckx, T. Jové, A. V. Shkumatov, A. Garcia-Pino, L. Geerts, M. De Kerpel, J. Lah, H. De Greve, L. Van Melderen, R. Loris, A unique hetero-hexadecameric architecture displayed by the *Escherichia coli* O157 PaaA2–ParE2 antitoxin–toxin complex. *J. Mol. Biol.* **428**, 1589–1603 (2016).

33. P. De Bruyn, Y. Girardin, R. Loris, Prokaryote toxin–antitoxin modules: Complex regulation of an unclear function. *Protein Sci.* **30**, 1103–1113 (2021).
34. R. Leplae, D. Geeraerts, R. Hallez, J. Guglielmini, P. Drèze, L. Van Melderen, Diversity of bacterial type II toxin–antitoxin systems: A comprehensive search and functional analysis of novel families. *Nucleic Acids Res.* **39**, 5513–5525 (2011).
35. M. Oberer, K. Zangger, K. Gruber, W. Keller, The solution structure of ParD, the antidote of the ParDE toxin–antitoxin module, provides the structural basis for DNA and toxin binding. *Protein Sci.* **16**, 1676–1688 (2007).
36. K. M. Dalton, S. Crosson, A conserved mode of protein recognition and binding in a ParD-ParE toxin-antitoxin complex. *Biochemistry* **49**, 2205–2215 (2010).
37. C. D. Aakre, J. Herrou, T. N. Phung, B. S. Perchuk, S. Crosson, M. T. Laub, Evolving new protein-protein interaction specificity through promiscuous intermediates. *Cell* **163**, 594–606 (2015).
38. Y. G. J. Sterckx, S. Haesaerts, L. Van Melderen, R. Loris, Crystallization and preliminary X-ray analysis of two variants of the *Escherichia coli* O157 ParE2–PaaA2 toxin–antitoxin complex. *Acta Crystallograp. Sec. F Struct. Biol. Commun.* **70**, 1284–1291 (2014).
39. T.-L. V. Lite, R. A. Grant, I. Nocedal, M. L. Littlehale, M. S. Guo, M. T. Laub, Uncovering the basis of protein-protein interaction specificity with a combinatorially complete library. *eLife* **9**, e60924 (2020).
40. K. J. Snead, L. L. Moore, C. R. Bourne, ParD antitoxin hotspot alters a disorder-to-order transition upon binding to its cognate ParE toxin, lessening its interaction affinity and increasing its protease degradation kinetics. *Biochemistry* **61**, 34–45 (2022).
41. L. Eberl, M. Givskov, H. Schwab, The divergent promoters mediating transcription of the par locus of plasmid RP4 are subject to autoregulation. *Mol. Microbiol.* **6**, 1969–1979 (1992).
42. T. L. Davis, D. R. Helinski, R. C. Roberts, Transcription and autoregulation of the stabilizing functions of broad-host-range plasmid RK2 in *Escherichia coli*, *Agrobacterium tumefaciens* and *Pseudomonas aeruginosa*. *Mol. Microbiol.* **6**, 1981–1994 (1992).
43. M. Gupta, N. Nayyar, M. Chawla, R. Sitaraman, R. Bhatnagar, N. Banerjee, The chromosomal parDE2 toxin–antitoxin system of *Mycobacterium tuberculosis* H37Rv: Genetic and functional characterization. *Front. Microbiol.* **7**, 1529 (2016).
44. G. Garcia-Rodriguez, Y. Girardin, A. N. Volkov, R. K. Singh, G. Muruganandam, J. Van Dyck, F. Sobott, W. Versées, D. Charlier, R. Loris, Entropic pressure controls the oligomerization of the *Vibrio cholerae* ParD2 antitoxin. *Acta Crystallogr D Struct Biol* **77**, 904–920 (2021).
45. M. Costa, M. Solà, G. del Solar, R. Eritja, A. M. Hernández-Arriaga, M. Espinosa, F. X. Gomis-Rüth, M. Coll, Plasmid transcriptional repressor CopG oligomerises to render helical superstructures unbound and in complexes with oligonucleotides. *J. Molec. Biol.* **310**, 403–417 (2001).
46. B. E. Raumann, M. A. Rould, C. O. Pabo, R. T. Sauer, DNA recognition by β-sheets in the Arc represser–operator crystal structure. *Nature* **367**, 754–757 (1994).
47. F. X. Gomis-Rüth, M. Solá, P. Acebo, A. Párraga, A. Guasch, R. Eritja, A. González, M. Espinosa, G. del Solar, M. Coll, The structure of plasmid-encoded transcriptional repressor CopG unliganded and bound to its operator. *EMBO J.* **17**, 7404–7415 (1998).
48. A. Talavera, H. Tamman, A. Ainelo, A. Konijnenberg, S. Hadži, F. Sobott, A. Garcia-Pino, R. Hõrak, R. Loris, A dual role in regulation and toxicity for the disordered N-terminus of the toxin GraT. *Nat. Commun.* **10**, 972 (2019).
49. A. Garcia-Pino, S. De Gieter, A. Talavera, H. De Greve, R. G. Efremov, R. Loris, An intrinsically disordered entropic switch determines allostery in Phd–Doc regulation. *Nat. Chem. Biol.* **12**, 490–496 (2016).
50. A. Vandervelde, I. Drobnak, S. Hadži, Y. G.-J. Sterckx, T. Welte, H. De Greve, D. Charlier, R. Efremov, R. Loris, J. Lah, Molecular mechanism governing ratio-dependent transcription regulation in the ccdAB operon. *Nucleic Acids Res.* **45**, 2937–2950 (2017).
51. D. Jurėnas, L. V. Melderen, A. Garcia-Pino, Mechanism of regulation and neutralization of the AtaR–AtaT toxin–antitoxin system. *Nat. Chem. Biol.* **15**, 285–294 (2019).
52. A. Bøggild, N. Sofos, K. R. Andersen, A. Feddersen, A. D. Easter, L. A. Passmore, D. E. Brodersen, The crystal structure of the intact *E. coli* RelBE toxin-antitoxin complex provides the structural basis for conditional cooperativity. *Structure* **20**, 1641–1648 (2012).
53. Y. Liu, Z. Gao, G. Liu, Z. Geng, Y. Dong, H. Zhang, Structural insights into the transcriptional regulation of HigBA toxin–antitoxin system by antitoxin HigA in *Pseudomonas aeruginosa*. *Front. Microbiol.* **10**, 3158 (2020).
54. M. C. Manav, K. J. Turnbull, D. Jurėnas, A. Garcia-Pino, K. Gerdes, D. E. Brodersen, The *E. coli* HicB antitoxin contains a structurally stable helix-turn-helix DNA binding domain. *Structure* **27**, 1675–1685.e3 (2019).
55. M. A. Schumacher, P. Balani, J. Min, N. B. Chinnam, S. Hansen, M. Vulić, K. Lewis, R. G. Brennan, HipBA–promoter structures reveal the basis of heritable multidrug tolerance. *Nature* **524**, 59–64 (2015).
56. M. J. Maté, R. Vincentelli, N. Foos, D. Raoult, C. Cambillau, M. Ortiz-Lombardía, Crystal structure of the DNA-bound VapBC2 antitoxin/toxin pair from Rickettsia felis. *Nucleic Acids Res.* **40**, 3245–3258 (2012).
57. G. V. Rajendrakumar, K. N. Ganesh, D. Chatterji, Interaction of the Mnt repressor with 37-base pair synthetic operator DNA fragments. Importance of symmetric GC pairs. *J. Biol. Chem.* **265**, 22300–22305 (1990).
58. A. K. Vershon, S.-M. Liao, W. R. McClure, R. T. Sauer, Bacteriophage P22 Mnt repressor. *J. Mol. Biol.* **195**, 311–322 (1987).
59. M. Overgaard, J. Borch, M. G. Jørgensen, K. Gerdes, Messenger RNA interferase RelE controls *relBE* transcription by conditional cooperativity. *Mol. Microbiol.* **69**, 841–857 (2008).
60. H. Qian, H. Yu, P. Li, E. Zhu, Q. Yao, C. Tai, Z. Deng, K. Gerdes, X. He, J. Gan, H.-Y. Ou, Toxin–antitoxin operon kacAT of Klebsiella pneumoniae is regulated by conditional cooperativity via a W-shaped KacA–KacT complex. *Nucleic Acids Res.* **47**, 7690–7702 (2019).
61. K. Mattison, J. S. Wilbur, M. So, R. G. Brennan, Structure of FitAB from *Neisseria gonorrhoeae* bound to DNA reveals a tetramer of toxin-antitoxin heterodimers containing pin domains and ribbon-helix-helix motifs. *J. Biol. Chem.* **281**, 37942–37951 (2006).
62. H. Afif, N. Allali, M. Couturier, L. V. Melderen, The ratio between CcdA and CcdB modulates the transcriptional repression of the ccd poison–antidote system. *Mol. Microbiol.* **41**, 73–82 (2001).
63. N. De Jonge, A. Garcia-Pino, L. Buts, S. Haesaerts, D. Charlier, K. Zangger, L. Wyns, H. De Greve, R. Loris, Rejuvenation of CcdB-poisoned gyrase by an intrinsically disordered protein domain. *Mol. Cell* **35**, 154–163 (2009).
64. W. P. C. Stemmer, A. Crameri, K. D. Ha, T. M. Brennan, H. L. Heyneker, Single-step assembly of a gene and entire plasmid from large numbers of oligodeoxyribonucleotides. *Gene* **164**, 49–53 (1995).
65. P. Nguyen Le Minh, C. Velázquez Ruiz, S. Vandermeeren, P. Abwoyo, I. Bervoets, D. Charlier, Differential protein-DNA contacts for activation and repression by ArgP, a LysR-type (LTTR) transcriptional regulator in *Escherichia coli*. *Microbiol. Res.* **206**, 141–158 (2018).
66. A. Schmitz, D. J. Galas, DNAase I footprinting: A simple method for the detection of protein-DNA binding specificity. *Nucleic Acids Res.* **5**, 3157–3170 (1978).
67. A. M. Maxam, W. Gilbert, "[57] Sequencing end-labeled DNA with base-specific chemical cleavages" in *Methods in Enzymology*, vol. 65 (Elsevier, 1980), pp. 499–560; https://linkinghub.elsevier.com/retrieve/pii/S0076687980650599.
68. A. Brunelle, R. F. Schleif, Missing contact probing of DNA-protein interactions. *Proc. Natl. Acad. Sci.* **84**, 6673–6676 (1987).
69. D. Charlier, "Chemical protection and premodification-binding interference for the identification of phosphate and base-specific contacts in protein–DNA complexes" in *Prokaryotic Gene Regulation*, vol. 2516 of Methods in Molecular Biology, E. Peeters, I. Bervoets, Eds., (Springer, 2022), pp. 201–237; https://link.springer.com/protocol/10.1007/978-1-0716-2413-5_12.
70. W. Kabsch, XDS. *Acta Crystallogr. Sec. D Biol. Crystallog.* **66**, 125–132 (2010).
71. Legrandp, Soleilproxima1, J. Aishima, CV-GPhL, legrandp/xdsme: March 2019 version working with the latest XDS version (Jan 26, 2018), version 0.6.6, Zenodo (2019).
72. D. Liebschner, P. V. Afonine, M. L. Baker, G. Bunkóczi, V. B. Chen, T. I. Croll, B. Hintze, L.-W. Hung, S. Jain, A. J. McCoy, N. W. Moriarty, R. D. Oeffner, B. K. Poon, M. G. Prisant, R. J. Read, J. S. Richardson, D. C. Richardson, M. D. Sammito, O. V. Sobolev, D. H. Stockwell, T. C. Terwilliger, A. G. Urzhumtsev, L. L. Videau, C. J. Williams, P. D. Adams, Macromolecular structure determination using X-rays, neutrons and electrons: Recent developments in *Phenix*. *Acta Crystallogr. Sec. D Struct. Biol.* **75**, 861–877 (2019).
73. P. Evans, Scaling and assessment of data quality. *Acta Crystallog. Sec. D Biolog. Crystallogr.* **62**, 72–82 (2006).
74. P. V. Afonine, R. W. Grosse-Kunstleve, N. Echols, J. J. Headd, N. W. Moriarty, M. Mustyakimov, T. C. Terwilliger, A. Urzhumtsev, P. H. Zwart, P. D. Adams, Towards automated crystallographic structure refinement with phenix.refine. *Acta Crystallogr. D Biol. Crystallogr.* **68**, 352–367 (2012).
75. P. Emsley, B. Lohkamp, W. G. Scott, K. Cowtan, Features and development of Coot. *Acta Crystallogr. D Biol. Crystallogr.* **66**, 486–501 (2010).
76. D. Franke, M. V. Petoukhov, P. V. Konarev, A. Panjkovich, A. Tuukkanen, H. D. T. Mertens, A. G. Kikhney, N. R. Hajizadeh, J. M. Franklin, C. M. Jeffries, D. I. Svergun, ATSAS 2.8: A comprehensive data analysis suite for small-angle scattering from macromolecular solutions. *J. Appl. Cryst.* **50**, 1212–1225 (2017).
77. C. D. Schwieters, J. J. Kuszewski, N. Tjandra, G. Marius Clore, The Xplor-NIH NMR molecular structure determination package. *J. Magn. Reson.* **160**, 65–73 (2003).
78. C. Schwieters, J. Kuszewski, G. Mariusclore, Using Xplor–NIH for NMR molecular structure determination. *Prog. Nucl. Magn. Reson. Spectrosc.* **48**, 47–62 (2006).
79. C. D. Schwieters, G. M. Clore, Using small angle solution scattering data in Xplor-NIH structure calculations. *Prog. Nucl. Magn. Reson. Spectrosc.* **80**, 1–11 (2014).
80. C. D. Schwieters, G. A. Bermejo, G. M. Clore, Xplor-NIH for molecular structure determination from NMR and other data sources. *Protein Sci.* **27**, 26–40 (2018).
81. J. Kuszewski, C. Schwieters, G. M. Clore, Improving the accuracy of NMR structures of DNA by means of a database potential of mean force describing base−base positional interactions. *J. Am. Chem. Soc.* **123**, 3903–3918 (2001).

82. G. M. Clore, J. Kuszewski, Improving the accuracy of NMR structures of RNA by means of conformational database potentials of mean force as assessed by complete dipolar coupling cross-validation. *J. Am. Chem. Soc.* **125**, 1518–1525 (2003).

Acknowledgments: We thank S. Haesaerts for technical assistance, A. Konijnenberg for help with native MS, Y. Sterckx for reading the manuscript, and J. Lah and S. Hadzi for discussions. **Funding:** This work was supported by FWO-Vlaanderen (grant nos. G.0226.17N and G.0033.20N to R.L.; and bursary no. 1164620N to Y.G.), Vrije Universiteit Brussel (grant no. SPR13 to R.L.), and iNEXT (grant no. 4146 to R.L.). **Author contributions:** Conceptualization: R.L., D.C., G.G.-R., and F.S. Methodology: R.L., D.C., G.G.-R., Y.G., A.N.V., and F.S. Investigation: G.G.-R., Y.G., D.C., R.K.S., J.V.D., and G.M. Resources: R.L., D.C., and J.V.D. Data curation: G.G.-R., Y.G., D.C., A.N.V., and F.S. Formal analysis: G.G.-R., Y.G., and A.N.V. Software: G.G.-R. and A.N.V. Validation: R.L., G.G.-R., R.K.S., J.V.D., G.M., D.C., A.N.V., and F.S. Project administration: R.L., D.C., and R.K.S. Visualization: G.G.-R., Y.G., A.N.V., D.C., J.V.D., and G.M. Funding acquisition: Y.G., R.L., and F.S. Supervision: R.L., D.C., and F.S. Writing—original draft: G.G.R., R.L., and D.C. Writing—review and editing: D.C., G.G.-R., R.L., Y.G., J.V.D., A.N.V., G.M., and F.S. **Competing interests:** The authors declare that they have no competing interests. **Data and materials availability:** All data needed to evaluate the conclusions in the paper are present in the paper and/or the Supplementary Materials. The PDB coordinates were deposited in the Protein Data Bank for the *Vc*ParD2:ParE2 complex with the accession code 7R5A. SAXS data were deposited in SASBDB (www.sasbdb.org/) with the following accession codes: SASDPN3, *Vc*ParD2:ParE2 antitoxin:toxin complex; SASDPK3, *Vc*ParD2:ParE2 complex bound to the 21-bp DNA operator box; SASDPL3, *Vc*ParD2:ParE2 complex bound to the 31-bp DNA operator box; and SASDPM3, *Vc*ParD2:ParE2 complex bound to the 33-bp DNA operator fragment. The ITC data are available in Supplemental Excel File.

Submitted 15 June 2023
Accepted 4 December 2023
Published 5 January 2024
10.1126/sciadv.adj2403